A High-Power Wireless Charging System Using *LCL*-N Topology to Achieve a Compact and Low-Cost Receiver

Yiming Zhang, *Member, IEEE*, Zhengchao Yan, *Student Member, IEEE*, Ziwei Liang, *Student Member, IEEE*, Siqi Li, *Member, IEEE*, and Chunting Chris Mi, *Fellow, IEEE*

***Abstract*—In high-power electric vehicle wireless charging systems, the charging distance is short, and the coupling is strong in order to increase the power density and reduce the coil size and the system cost. With a strong coupling, the receiver-side compensation can be eliminated, and a high efficiency can still be obtained. The inductor-capacitor-inductor-none (*LCL*-N) topology is formed with the *LCL* compensation on the primary side. The phase difference between the transmitter and receiver currents is larger than 90°, leading to the magnetic flux cancelation in the ferrites. Thus, the required ferrite thickness of the *LCL*-N topology is smaller than the fully-compensated topologies. Therefore, a compact, lightweight, and low-cost receiver structure is achieved with the omitted compensation and thinner ferrite. Moreover, the *LCL*-N topology can achieve zero voltage switching for all loading conditions, withstand open-circuit and short-circuit faults, and is suitable for constant-current and constant-voltage charging due to the fact that it has neither a CC nor a CV output characteristic. A 100-kW system is designed and simulated. A downscaled 1-kW system is implemented. The simulations and experimental results verify the effectiveness of the analysis.**

***Index Terms*—Compact receiver, inductor-capacitor-inductor-none (*LCL*-N) topology, magnetic flux cancellation, wireless charging, wireless power transfer (WPT).**

Manuscript received January 24, 2019; accepted April 25, 2019. Date of publication May 1, 2019; date of current version October 18, 2019. This work was supported in part by Huawei Technologies Co. Ltd under Grant 9406139, and in part by the Department of Energy, Argonne National Laboratory, US–China Clean Energy Center under Grant DE-AC02-06CH11357. Recommended for publication by Associate Editor U. K. Madawala. *(Corresponding author: Chunting Chris Mi.)*

Y. Zhang and C. C. Mi are with the Department of Electrical and Computer Engineering, San Diego State University, San Diego, CA 92182 USA (e-mail: zhangym07@gmail.com; mi@ieee.org).

Z. Yan is with the School of Marine Science and Technology, Northwestern Polytechnical University, Xi'an 710072, China, and also with the Department of Electrical and Computer Engineering, San Diego State University, San Diego, CA 92182 USA (e-mail: yanzc1991@gmail.com).

Z. Liang is with the School of Electrical Engineering, Beijing Jiaotong University, Beijing 100044, China, and also with the Department of Electrical and Computer Engineering, San Diego State University, San Diego, CA 92182 USA (e-mail: 16121472@bjtu.edu.cn).

S. Li is with the School of Electrical Engineering, Kunming University of Science and Technology, Kunming 650101, China, and also with the Department of Electrical and Computer Engineering, San Diego State University, San Diego, CA 92182 USA (e-mail: lisiqi@kmust.edu.cn).

Color versions of one or more of the figures in this paper are available online at http://ieeexplore.ieee.org.

Digital Object Identifier 10.1109/TPEL.2019.2914363

I. Introduction

ELECTRIC vehicles (EVs) or hybrid EVs are the future trends of vehicle development to get rid of fossil fuels and become environmentally friendly. The global stock of EVs was over 3 million in 2017, an increase of 57% from the previous year [1]. User-unfriendly charging experience, such as the inconvenience of manually plugging an EV cord into a charging port and long charging time, should be solved for further penetration of EVs into the commercial market.

Wireless power transfer (WPT) can eliminate the connection between the source and the load for convenience, safety, reliability, and feasibility in certain applications [2]–[5]. On the other hand, the charging time can be greatly reduced with high-power charging technique. Therefore, the high-power WPT technology should be developed to enhance the user-friendly charging experience of EVs.

In kilo-watt WPT systems for EVs, the charging distance is normally between 100 and 250 mm, achieving a coupling coefficient of the transmitting and receiving coils in the range of 0.3–0.1 [6]–[8]. As for high-power WPT systems over 50 kW, a compact, lightweight, and low-cost receiver is crucial to the application of the high-power WPT technology. Mechanical equipment can be utilized for positioning and adjusting the charging distance within 50 mm, to improve power density and achieve a compact and lightweight structure, especially for the receiver side [9]–[11]. The coupling coefficient of the transmitter and the receiver can be over 0.70 within a distance of 50 mm.

Compensations are utilized in WPT systems to improve efficiency and reduce the volt-ampere rating of the power electronics converters. There are four popular compensations in WPT systems, namely series (S), parallel (P), inductor-capacitor-inductor (*LCL*), and inductor-capacitor-capacitor (*LCC*). *LCL* and *LCC* compensations are basically the same except that a capacitor is inserted in the main coil branch in the *LCC* compensation to block the dc component of the source and offer an extra degree of freedom to design a WPT system. *LCL* can be regarded as a special case for *LCC* when the inserted capacitor is infinite or eliminated. Here take the *LCL* compensation as an example. Presently the voltage-source inverter (VSI) is overwhelmingly employed as the source in WPT systems compared with the current source inverter. The P compensation cannot be directly connected to the VSI due to the fact that two voltage

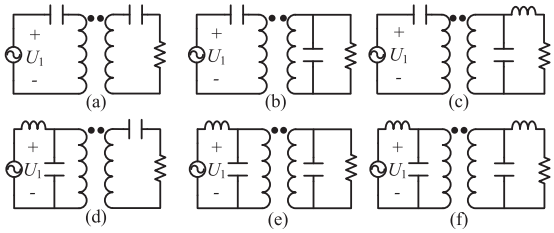

Fig. 1. Compensation topologies. (a) SS. (b) SP. (c) S-*LCL*. (d) *LCL*-S. (e) *LCL*-P. (f) *LCL*–*LCL*.

TABLE I
OUTPUT CHARACTERISTICS OF SIX TOPOLOGIES

Topology	Output Characteristic	Topology	Output Characteristic
SS	CC	LCL-S	CV
SP	CV	LCL-P	CC
S-LCL	CV	LCL-LCL	CC

sources cannot be connected in parallel. Thus, there are two kinds of compensations on the transmitter side: S and *LCL*. For the receiver side, there are three kinds of compensations: S, P, and *LCL*. With the combination of different transmitter-side and receiver-side compensations, there are six topologies in WPT systems: SS [12], SP [13], S-*LCL* [14], *LCL*-S [15], *LCL*-P [16], [17], and *LCL*–*LCL* [18], shown in Fig. 1. At resonance, the output characteristics of these six topologies, namely constant-current (CC) or constant-voltage (CV) output characteristics, are given in Table I. The CC output characteristic indicates that the output current is independent of the loading condition and the CV output characteristic means that the output voltage keeps constant with the load variation. Detailed descriptions can be found in [19].

Note that when the capacitors in the SS topology resonate with the leakage inductances, the SS topology has a CV output. For the topologies with a CC output, overvoltage will occur when open-circuit (OC) fault happens on the receiver side, leading to the system breakdown. For the topologies with a CV output, overcurrent will occur when short-circuit (SC) fault happens on the receiver side, also leading to the system breakdown. Therefore, special attention should be paid to the OC and SC faults, especially for high-power WPT systems, where the system breakdown can be disastrous.

To reduce the volume and cost of the receiver, the receiver-side compensation was eliminated in [20], forming a series-none (SN) topology with the transmitter-side S compensation. The SN topology has a CV output, making it difficult to control the charging current if there is no dc–dc converter on the receiver side, which is often eliminated to achieve a simple receiver. Moreover, the SN topology cannot withstand the SC fault due to its CV output. To solve these problems, an *LCL*-none (*LCL*-N) topology for a high-power strongly coupled WPT system is proposed in this paper, where the transmitter-side compensation is *LCL* for achieving a CC on the transmitting coil and the receiver-side compensation is eliminated to reduce the weight, cost, and volume of the receiver. It is found that the thickness of the receiver ferrite can be reduced due to the fact that the phase difference between the transmitter and receiver coil currents is larger than 90°, leading to magnetic flux cancellation in the ferrite. Thus, the receiver size, weight, and cost are further decreased. Moreover, the *LCL*-N topology can withstand receiver-side OC and SC faults. A 100-kW WPT system is designed and simulated. A downscaled prototype is implemented to validate the analysis.

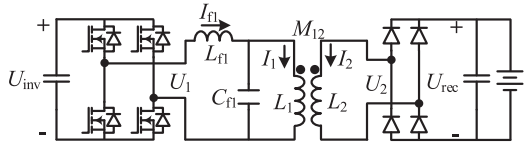

Fig. 2. *LCL*-N topology of the WPT system.

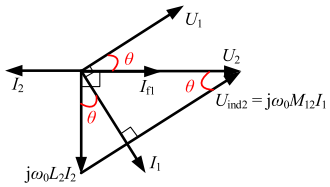

Fig. 3. Phasor diagram of the *LCL*-N topology.

II. MODELING AND ANALYSIS

A. Modeling

The *LCL*-N topology of a high-power wireless charging system for EVs is depicted in Fig. 2. The load is a battery, denoted by a voltage source, and there is no dc–dc converter on the receiver side. $U_{\rm inv}$ ($U_{\rm rec}$) and U_1 (U_2) are the inverter (rectifier) dc and ac voltages, respectively; L_{f1} (C_{f1}) is the compensation inductance (capacitance); L_1 (L_2) is the transmitter (receiver) inductance; M_{12} is the mutual inductance; I_1 (I_2) is the transmitter (receiver) current; and I_{f1} is the compensation inductor current. U_1 can be regulated for a target output by either doing phase shift control or changing $U_{\rm inv}$.

In the *LCL*-N topology, the transmitter side alone is set to be in resonance. Thus, we have $L_{f1} = L_1$ and

$$\omega_0 = \frac{1}{\sqrt{L_{f1}C_{f1}}} = \frac{1}{\sqrt{L_1 C_{f1}}}. \tag{1}$$

Based on first harmonic approximation (FHA), we have

$$U_1 = \frac{2\sqrt{2}}{\pi}U_{\rm inv}, \quad U_2 = \frac{2\sqrt{2}}{\pi}U_{\rm rec}. \tag{2}$$

The model of the *LCL*-N topology can be established as

$$\begin{cases} \boldsymbol{U_1} = j\omega_0 L_{f1}\boldsymbol{I_{f1}} + j\omega_0 L_1 \boldsymbol{I_1} + j\omega_0 M_{12}\boldsymbol{I_2} \\ \boldsymbol{U_2} = j\omega_0 L_2 \boldsymbol{I_2} + j\omega_0 M_{12}\boldsymbol{I_1} \\ \boldsymbol{I_{f1}} = \boldsymbol{I_1} + j\omega_0 C_{f1}\left(j\omega_0 L_1 \boldsymbol{I_1} + j\omega_0 M_{12}\boldsymbol{I_2}\right) \end{cases} \tag{3}$$

where the parameters in bold represent the phasor quantities.

The phasor diagram of the *LCL*-N topology is depicted in Fig. 3, where θ is the phase difference between U_1 and I_{f1} and $U_{\rm ind2}$ is the induced voltage on the receiving coil. U_1 leads I_{f1},

indicating that zero voltage switching can be achieved for the *LCL*-N topology.

The coil currents can be calculated as

$$I_1 = \frac{U_1}{\omega_0 L_1} \tag{4}$$

$$I_2 = \frac{1}{\omega_0 L_2}\sqrt{\left(\frac{M_{12}}{L_1}U_1\right)^2 - U_2^2} \tag{5}$$

$$I_{f1} = \frac{M_{12}}{L_1} I_2. \tag{6}$$

The output power can be expressed as

$$P_{\text{out}} = \frac{U_2}{\omega_0 L_2}\sqrt{\left(\frac{M_{12}}{L_1}U_1\right)^2 - U_2^2}. \tag{7}$$

Compared with the equivalent resistances of the coils, the equivalent series resistances of the capacitors can be ignored. Assuming the equivalent resistances of L_{f1}, L_1, and L_2 are R_{f1}, R_1, and R_2, respectively, the coil-to-coil efficiency is

$$\eta_{\text{coil}} = \frac{P_{\text{out}}}{P_{\text{out}} + I_{f1}^2 R_{f1} + I_1^2 R_1 + I_2^2 R_2}. \tag{8}$$

B. Induced Voltage

The induced voltage on the receiving coil is

$$U_{\text{ind2}} = \omega_0 M_{12} I_1 = \frac{M_{12}}{L_1}U_1 = k_{12}\sqrt{\frac{L_2}{L_1}}U_1 \tag{9}$$

where k_{12} is the coupling coefficient. When U_{ind2} is not significantly larger than U_2, I_2 will be discontinuous.

According to Fig. 3, the power factor of the transmitter can be expressed as

$$\cos\theta = \frac{U_2}{U_{\text{ind2}}} = \sqrt{\frac{L_1}{L_2}}\frac{U_2}{k_{12}U_1}. \tag{10}$$

To increase the power factor of the inverter, U_{ind2} should be small. Thus, L_2 should be smaller than L_1. However, when U_{ind2} is small, I_2 will be discontinuous, resulting in large root-mean-square value of I_2 for the same output power. Therefore, there is a tradeoff between large I_{f1} caused by low power factor and large I_2 caused by the discontinuous waveform.

C. Magnetic Flux Cancellation

It should be noted from Fig. 3 that the phase difference between I_1 and I_2 is $\varphi_{12} = 90° + \theta$, which is larger than 90°. The magnetic field in the ferrite generated by the transmitter and receiver currents will cancel each other to a large extent and the required ferrite thickness will be reduced.

The decomposition of the transmitter current is shown in Fig. 4, where I_{11} is the component perpendicular to I_2 and I_{12} is the component out of phase with I_2. The cross product of I_1 and I_2, which is the product of I_{11} and I_2, contributes to the power transfer. As for I_{12}, since it is out of phase with I_2 and the transmitting and receiving coils are close to each other, the magnetic flux in the ferrite generated by I_{12} and I_2 will cancel each other. Therefore, the magnetic flux density both in the transmitter and receiver ferrites when $\varphi_{12} > 90°$ will be smaller than that when $\varphi_{12} = 90°$.

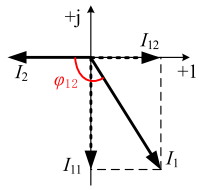

Fig. 4. Current phasor diagram with the decomposition of transmitter current.

D. Output Characteristic

Based on the Pythagorean Theorem of the triangle in Fig. 3, the relationship between U_2 and I_2 can be expressed as

$$U_2^2 + (\omega_0 L_2 I_2)^2 = (\omega_0 M_{12} I_1)^2 = \left(\frac{M_{12}}{L_1}U_1\right)^2. \tag{11}$$

We can see from (11) that the output voltage U_2 and the output current I_2 are coupled with each other. That means for the *LCL*-N topology, it has neither a CV nor a CC output. Thus, it can be suitable for CV and CC charging by tuning U_1.

The OC voltage on the receiver side can be obtained by letting $I_2 = 0$ in (11), namely

$$U_{2-\text{OC}} = \frac{M_{12}}{L_1}U_1 = U_{\text{ind2}} \tag{12}$$

which is the same as the induced voltage on the receiver side for the normal operation. $U_{2\text{-OC}}$ is on the same order of U_1 and U_2, which can be tolerated by the receiver.

With the OC fault, I_{f1} is close to zero and I_1 is still solely dependent on U_1 and can be expressed as

$$I_{1-\text{OC}} = \frac{U_1}{\omega_0 L_1} = I_1 \tag{13}$$

which is the same as the normal operation. In fact, this is the characteristic of the primary-side *LCL* compensation that the transmitting coil current keeps constant regardless of the receiver-side loading condition.

Similarly, the SC current on the receiver side can be obtained by letting $U_2 = 0$ in (4)–(6), namely

$$I_{1-\text{SC}} = \frac{U_1}{\omega_0 L_1} = I_1 \tag{14}$$

$$I_{2-\text{SC}} = \frac{M_{12}U_1}{\omega_0 L_1 L_2} = \frac{I_2}{\sqrt{1-\left(\frac{L_1 U_2}{M_{12}U_1}\right)^2}} = \frac{I_2}{\sqrt{1-\left(\frac{U_2}{U_{\text{ind2}}}\right)^2}} \tag{15}$$

$$I_{f1-\text{SC}} = \frac{M_{12}}{L_1} I_{2-\text{SC}} = \frac{I_{f1}}{\sqrt{1-\left(\frac{L_1 U_2}{M_{12}U_1}\right)^2}} = \frac{I_{f1}}{\sqrt{1-\left(\frac{U_2}{U_{\text{ind2}}}\right)^2}}. \tag{16}$$

$I_{1\text{-SC}}$ keeps the same as I_1. $I_{2\text{-SC}}$ and I_{f1-SC} increase. Due to the fact that U_{ind2} should not be close to U_2 to allow for the conduction of the rectifier, U_2/U_{ind2} is smaller but not close to

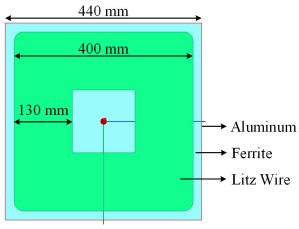

Fig. 5. Coil dimension for 100-kW system.

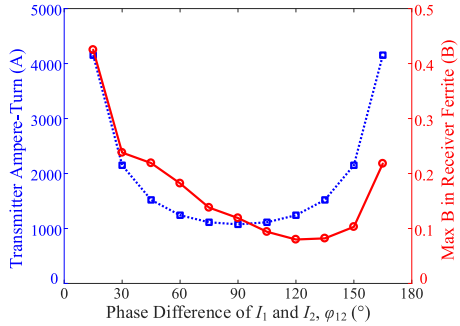

Fig. 6. Transmitter ampere-turn and maximum magnetic flux density versus phase difference of I_1 and I_2.

1. Thus, $I_{2\text{-SC}}$ and I_{f1-SC} are also on the same order of I_2 and I_{f1}. They can be restricted to be within twice the values of I_2 and I_{f1} as long as $U_{\text{ind2}} > 1.118U_2$. Thus, the SC currents can also be tolerated by the transmitter and the receiver.

Therefore, the *LCL*-N topology can withstand OC and SC faults.

III. Design of the 100-kW WPT System

A. Design

The transferred power of two coupled coils can be expressed as [21]

$$P_{\text{out}} = \omega_0 M_{12} I_1 I_2 \sin\varphi_{12} = \omega_0 k_{12}\sqrt{L_{10}L_{20}}\,(n_1 I_1)\,(n_2 I_2)\sin\varphi_{12} \tag{17}$$

where L_{10} (L_{20}), n_1 (n_2), and $n_1 I_1$ ($n_2 I_2$) are the single-turn inductance, the turn number, and the ampere-turn of the transmitter (receiver).

For the 100-kW WPT system, the coils are designed to be symmetrical, whose dimension is shown in Fig. 5. The charging distance is 35 mm. The simulated coupling coefficient is 0.82 and the single-turn self-inductances L_{10} and L_{20} are 0.84 μH.

For the fully compensated topologies such as SS and *LCL–LCL*, φ_{12} is 90°. When $n_1 I_1 = n_2 I_2$, the required ampere-turn amplitudes of the transmitter and the receiver for the 100-kW system can be calculated as

$$(n_1 I_1)_{\text{amp}} = (n_2 I_2)_{\text{amp}} = \sqrt{2}\cdot\sqrt{\frac{P_{\text{out}}}{\omega_0 k_{12}\sqrt{L_{10}L_{20}}}} = 1075A. \tag{18}$$

To investigate the impact of φ_{12} on the magnetic flux density in the receiver ferrite, the receiver ampere-turn amplitude is fixed as 1075 A and φ_{12} is varied. For the same output power, the required transmitter ampere-turn amplitude can be calculated as

$$(n_1 I_1)_{\text{amp}} = \frac{(n_2 I_2)_{\text{amp}}}{\sin\varphi_{12}}. \tag{19}$$

The model is built in ANSYS/Maxwell. The receiver ampere-turn amplitude is set as 1075 A. The transmitter ampere-turn amplitude and the simulated maximum magnetic flux density in the receiver ferrite varying with φ_{12} are depicted in Fig. 6. When φ_{12} is 90°, the transmitter ampere-turn amplitude is minimized, equal to 1075 A. However, the magnetic flux density in the receiver ferrite is not the minimum in this condition. When φ_{12} is in the proximity of 140°, the simulated magnetic flux density in the receiver ferrite is minimized, at the expense of increasing the ampere-turn of the transmitter. Therefore, for the same output power, the phase difference between the transmitter and receiver coil currents should be larger than 90°, typically around 140°, to reduce the receiver ferrite thickness. In the *LCL*-N topology, φ_{12} is larger than 90° and can be designed to be around the optimal value. Thus, the receiver ferrite thickness of the *LCL*-N topology can be further decreased compared with the fully compensated topologies, such as SS and *LCL–LCL*, leading to a low-cost, lightweight, and compact receiver.

TABLE II
Parameters and Simulated Results for 100-kW *LCL*-N Topology

Parameter	Value	Parameter	Value
L_{fl} (L_1, L_2)	3.36 μH	U_{inv}	692 V
C_{fl}	4.71 μF	I_{fl}	355 A
f	40 kHz	I_1	746 A
k	0.82	I_2	432 A
M_{12}	2.76 μH	P_{out}	100 kW
U_{rec}	300 V	η	97.73%

In the *LCL*-N topology, the battery pack is directly connected to the rectifier through a filter without any dc–dc converter for simplicity and low cost on the receiver side. The battery voltage is 300 V and the maximum inverter dc voltage is set as 700 V. The operating frequency is 40 kHz. For a symmetrical system when $L_1 = L_2$, the required inductance valued can be obtained according to (7) as

$$L_2 = \frac{U_2}{\omega_0 P_{\text{out}}}\sqrt{(k_{12}U_1)^2 - U_2^2} = 4.73\ \mu\text{H}. \tag{20}$$

Considering the discontinuousness of the rectifier current, the required inductance values should be smaller than the calculated ones. The coil dimensions are the same as shown in Fig. 5. The transmitter ferrite thickness is 12 mm and the receiver ferrite thickness is 9 mm due to the magnetic flux cancellation with the phase difference of I_1 and I_2 larger than 90°. The turn numbers of coils are chosen as 2. Thus, $L_{f1} = L_1 = L_2 = 3.36\ \mu$H. C_{f1} is calculated as 4.71 μF.

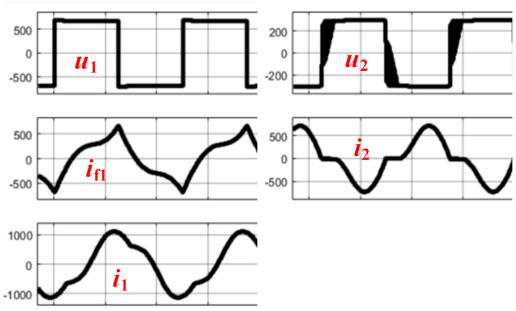

Fig. 7. Simulated voltage and current waveforms of the *LCL*-N topology.

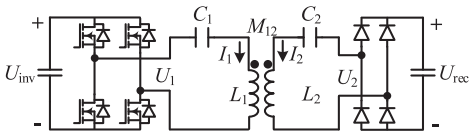

Fig. 8. SS topology of the WPT system.

TABLE III
PARAMETERS AND SIMULATED RESULTS FOR 100-kW SS TOPOLOGY

Parameter	Value	Parameter	Value
L_1 (L_2)	7.56 μH	U_{inv}	568 V
C_1 (C_2)	2.09 μF	I_1	259 A
f	40 kHz	I_2	371 A
k	0.82	P_{out}	100 kW
M_{12}	6.20 μH	η	97.92%
U_{rec}	300 V		

B. Simulation

The model is built in MATLAB/Simulink. The parameters and the simulated results are given in Table II and the simulation waveforms are displayed in Fig. 7.

Considering the fundamental component, the phase difference between I_1 and I_2 is approximately 150°, which is close to the calculation based on (10). The simulated magnetic flux density in the transmitter and receiver ferrites is restricted to be within 0.12 T when the transmitter and receiver ferrite thicknesses are 12 and 9 mm, respectively.

C. Comparison

Both the *LCL–LCL* and *LCC–LCC* topology would introduce more cost and weight than the *LCL*-N or SS topology due to more passive elements. Here, only the *LCL*-N and the SS topologies are compared for the cost and weight.

The SS topology is depicted in Fig. 8, where C_1 and C_2 are the compensation capacitances.

The same coil geometry is applied to the SS topology except that the turn number is 3 to match the dc voltage ranges of the inverter and the rectifier. The model is also built in MATLAB/Simulink. The parameters and simulated results are shown in Table III.

The energy stored in the coil or the capacitor is taken as the indicator for the cost and weight of the copper material or the capacitor, namely

$$E_{\text{Copper}} = \frac{1}{2}LI^2, \quad E_{\text{Cap}} = \frac{1}{2}CU^2. \tag{21}$$

To restrain the magnetic flux density to be within 0.12 T, the required transmitter and receiver ferrite thicknesses are both 14 mm, respectively.

Take the SS topology as the base. The comparison of the per-unit values of the related materials in the SS and *LCL*-N topologies is given in Table IV. Compared with the SS topology, the receiver-side cost and weight of the *LCL*-N topology are greatly reduced at the expense of increasing the transmitter-side cost and weight. Still it is beneficial because the vehicle-side cost and weight are more of a concern than that of the ground side and one transmitter can charge multiple EVs during different time periods for a full utilization. Moreover, the *LCL*-N topology can withstand the OC and SC faults, making it a suitable topology for high-power strongly coupled WPT systems.

TABLE IV
COMPARISON OF SS AND *LCL*-N TOPOLOGIES

Topology		SS	LCL-N
Transmitter	Copper	1	4.52
	Ferrite	1	0.86
	Capacitor	1	2.90
Receiver	Copper	1	0.60
	Ferrite	1	0.64
	Capacitor	1	0

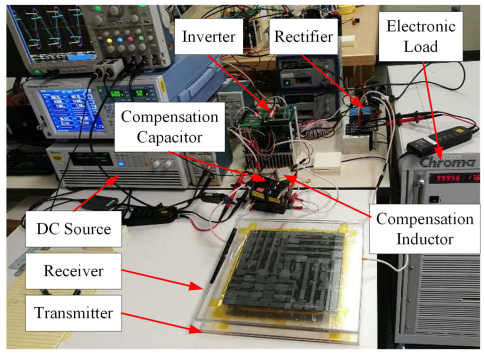

Fig. 9. Photograph of experimental prototype.

TABLE V
PARAMETERS OF EXPERIMENTAL PROTOTYPE

Parameter	Value	Parameter	Value
L_{f1} (L_1, L_2)	63.5 μH	C_{f1}	54.7 nF
M_{12}	568 V	k	0.80
f	85.4 kHz		

IV. IMPLEMENTATION OF DOWNSCALED SYSTEM

A downscaled experimental prototype of the *LCL*-N topology is implemented to validate the analysis, shown in Fig. 9. The parameters are given in Table V.

A simulation model based on MATLAB/Simulink is also built. U_{rec} is set to 100 V. U_{inv} is adjusted for different output powers. The calculations, simulations, and experimental results

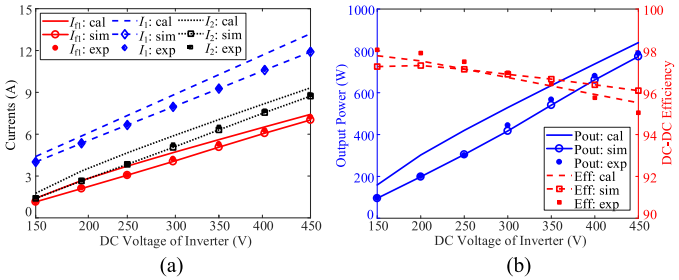

Fig. 10. Calculations, simulations, and experimental results versus $U_{\rm inv}$. (a) Coil currents. (b) Output power and dc–dc efficiency.

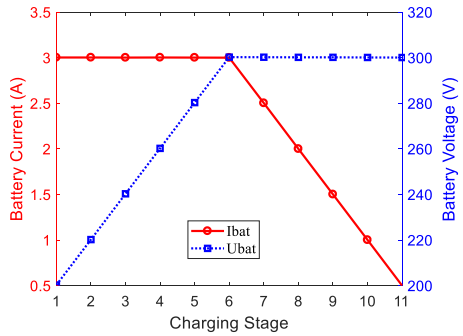

Fig. 11. Charging profile of CC and CV charging.

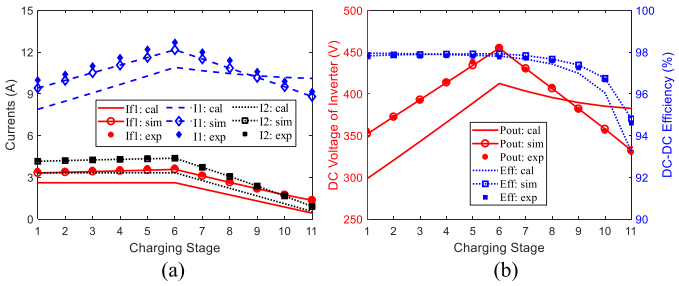

Fig. 12. Calculations, simulations, and experimental results versus charging stage. (a) Coil currents. (b) Output power and dc–dc efficiency.

of the coil currents, the output power, and the dc–dc efficiency varying with $U_{\rm inv}$ are shown in Fig. 10. We can see that the simulations are in good agreement with the experimental results. The mismatches of the calculations are caused by the distorted currents. FHA is no longer accurate.

A charging profile is performed to simulate CC and CV charging, as shown in Fig. 11. The calculations, simulations, and experimental results of the coil currents, the output power, and the dc–dc efficiency varying with the charging stage are shown in Fig. 12. Similarly, the simulations match the experimental results well. The mismatches of the calculations are also caused by the distorted waveforms. Nevertheless, the trends predicted by FHA still offer valuable information on the characteristics of the *LCL*-N topology. We can see from Fig. 12 that $U_{\rm inv}$ can be regulated for CC and CV charging.

With small $U_{\rm inv}$, $U_{\rm ind2}$ is small and I_2 is discontinuous. With large $U_{\rm inv}$, $U_{\rm ind2}$ is large and I_2 is continuous. In the experimental setup of the same coil inductances, when $U_{\rm ind2}$ is below

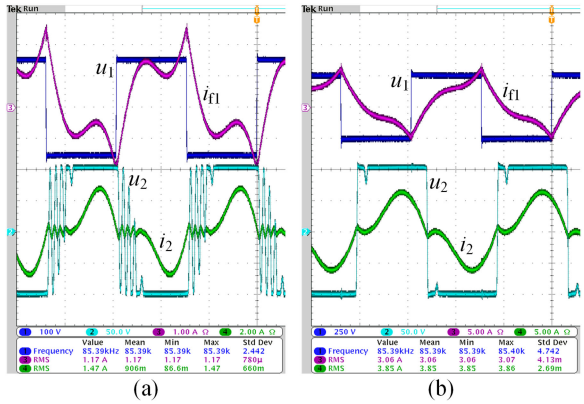

Fig. 13. Voltage and current waveforms. (a) $U_{\rm inv} = 150$ V and $U_{\rm rec} = 100$ V. (b) $U_{\rm inv} = 250$ V and $U_{\rm rec} = 100$ V.

twice the value of U_2, or $U_{\rm inv}$ is below 2.5 times the value of $U_{\rm rec}$, I_2 will be discontinuous. The experimental waveforms of the two cases corresponding to the discontinuous and continuous receiver currents are displayed in Fig. 13.

V. Conclusion

In this paper, an *LCL*-N topology is proposed for a high-power strongly coupled WPT system with a compact, lightweight, and low-cost receiver. The *LCL* compensation is utilized on the transmitter side and there is no compensation on the receiver side. The model of the *LCL*-N topology is built. The *LCL*-N topology has neither a CC nor a CV output characteristic. Thus, it can withstand OC and SC faults and is suitable for CC and CV charging. Due to the fact that the phase difference between the transmitting and receiving coil currents is larger than 90° in the *LCL*-N topology, the magnetic flux density in the ferrite generated by the transmitting and receiving coil currents will cancel each other and the required receiver ferrite thickness can be reduced. Therefore, without any compensation on the receiver side and with reduced receiver ferrite thickness, a compact, lightweight, and low-cost receiver for a strongly coupled WPT system can be achieved at the expense of larger transmitter-side cost and weight. Because the coupling is strong, the efficiency can be high even though there is no compensation on the receiver side.

A 100-kW WPT system based on the *LCL*-N topology is designed and simulated. A downscaled 1-kW WPT system is implemented. The calculations, simulations, and experimental results validate the effectiveness of the analysis.

References

[1] "Global electric vehicle market outlook 2018," Int. Energy Agency, Paris, France, 2018.
[2] Z. Yan *et al.*, "Frequency optimization of a loosely coupled underwater wireless power transfer system considering eddy current loss," *IEEE Trans. Ind. Electron.*, vol. 66, no. 5, pp. 3468–3476, May 2019.
[3] Y. Zhang, Z. Zhao, and T. Lu, "Quantitative analysis of system efficiency and output power of four-coil resonant wireless power transfer," *IEEE J. Emerg. Sel. Top. Power Electron.*, vol. 3, no. 1, pp. 184–190, Mar. 2015.
[4] T. Kan, Y. Zhang, Z. Yan, P. Mercier, and C. C. Mi, "A rotation-resilient wireless charging system for lightweight autonomous underwater vehicles," *IEEE Trans. Veh. Technol.*, vol. 67, no. 8, pp. 6935–6942, Aug. 2018.

[5] Y. Zhang, *Key Technologies of Magnetically-Coupled Resonant Wireless Power Transfer*. Singapore: Springer, 2017.
[6] Z. Li, C. Zhu, J. Jiang, K. Song, and G. Wei, "A 3-kW wireless power transfer system for sightseeing car supercapacitor charge," *IEEE Trans. Power Electron.*, vol. 32, no. 5, pp. 3301–3316, May 2017.
[7] S. Y. Choi, J. Huh, W. Y. Lee, and C. T. Rim, "Asymmetric coil sets for wireless stationary EV chargers with large lateral tolerance by dominant field analysis," *IEEE Trans. Power Electron.*, vol. 29, no. 12, pp. 6406–6420, Dec. 2014.
[8] Y. Yao, Y. Wang, X. Liu, F. Lin and D. Xu, "A novel parameter tuning method for a double-sided LCL compensated WPT system with better comprehensive performance," *IEEE Trans. Power Electron.*, vol. 33, no. 10, pp. 8525–8536, Oct. 2018.
[9] A. Foote and O. C. Onar, "A review of high-power wireless power transfer," in *Proc. IEEE Trans. Electrif. Conf. Expo*, 2017, pp. 234–240.
[10] Z. Bi, T. Kan, C. C. Mi, Y. Zhang, Z. Zhao, and G. A. Keoleian, "A review of wireless power transfer for electric vehicles: Prospects to enhance sustainable mobility," *Appl. Energy*, vol. 179, no., pp. 413–425, 2016.
[11] "Charging electric buses quickly and efficiently: Bus stops fitted with modular components make "Charge & Go" simple to implement," Conductix-Wampfler, Omaha, NE, USA, 2013. [Online]. Available: http://www.conductix.us/en/news/2013-05-29/charging-electric-buses-quickly-and-efficiently-bus-stops-fitted-modular-components-make-charge-go
[12] F. Liu, Y. Yang, Z. Ding, X. Chen, and R. M. Kennel, "A multifrequency superposition methodology to achieve high efficiency and targeted power distribution for a multiload MCR WPT system," *IEEE Trans. Power Electron.*, vol. 33, no. 10, pp. 9005–9016, Oct. 2018.
[13] M. Chinthavali and Z. J. Wang, "Sensitivity analysis of a wireless power transfer (WPT) system for electric vehicle application," in *Proc. IEEE Energy Convers. Congr. Expo.*, 2016, pp. 1–8.
[14] R. Mai, Y. Chen, Y. Zhang, N. Yang, G. Cao, and Z. He, "Optimization of the passive components for an S-LCC topology-based WPT system for charging massive electric bicycles," *IEEE Trans. Ind. Electron.*, vol. 65, no. 7, pp. 5497–5508, Jul. 2018.
[15] C. Xiao, D. Cheng, and K. Wei, "An LCC-C compensated wireless charging system for implantable cardiac pacemakers: Theory, experiment, and safety evaluation," *IEEE Trans. Power Electron.*, vol. 33, no. 6, pp. 4894–4905, Jun. 2018.
[16] W. Li, H. Zhao, T. Kan, and C. Mi, "Inter-operability considerations of the double-sided LCC compensated wireless charger for electric vehicle and plug-in hybrid electric vehicle applications," in *Proc. IEEE PELS Workshop Emerg. Technol., Wireless Power*, 2015, pp. 1–6.
[17] Z. Yan, Y. Zhang, B. Song, K. Zhang, T. Kan, and C. Mi, "An LCC-P compensated wireless power transfer system with a constant current output and reduced receiver size," *Energies*, vol. 12, no. 1, p. 172, Jan. 2019.
[18] S. Li, W. Li, J. Deng, T. D. Nguyen, and C. Mi, "A double-sided LCC compensation network and its tuning method for wireless power transfer," *IEEE Trans. Veh. Technol.*, vol. 64, no. 6, pp. 2261–2273, Jun. 2015.
[19] W. Zhang and C. C. Mi, "Compensation topologies of high-power wireless power transfer systems," *IEEE Trans. Veh. Technol.*, vol. 65, no. 6, pp. 4768–4778, Jun. 2016.
[20] Y. Zhang, T. Kan, Z. Yan, Y. Mao, Z. Wu, and C. Mi, "Modeling and analysis of series-none compensation for wireless power transfer systems with a strong coupling," *IEEE Trans. Power Electron.*, vol. 34, no. 2, pp. 1209–1215, Feb. 2019.
[21] S. Li and C. Mi, "Wireless power transfer for electric vehicle applications," *IEEE J. Emerg. Sel. Top. Power Electron.*, vol. 3, no. 1, pp. 4–17, Mar. 2015.

Yiming Zhang (S'13–M'16) received the B.S. and Ph.D. degrees in electrical engineering from Tsinghua University, Beijing, China, in 2011 and 2016, respectively.

He is currently a Postdoctoral Researcher with San Diego State University, San Diego, CA, USA. His research interests include wireless power transfer for electric vehicles and mobile phones, and resonant converters.

Zhengchao Yan (S'18) received the B.S. degree in mechanical design, manufacturing, and automation in 2013 from Northwestern Polytechnical University, Xi'an, China, where he is currently working toward the Ph.D. degree.

In 2017, he received the funding from China Scholarship Council, and became a joint Ph.D. student with the Department of Electrical and Computer Engineering, San Diego State University, San Diego, CA, USA. His research interests include wireless power transfer, including coil design and compensation topologies.

Ziwei Liang (S'18) received the B.S. degree in electrical engineering in 2016 from China University of Mining and Technology, Xuzhou, China. He is currently working toward the M.S. degree in electrical engineering at Beijing Jiaotong University, Beijing, China.

He received the funding from Beijing Jiaotong University and used to be a Joint Student with the Department of Electrical and Computer Engineering, San Diego State University, San Diego, CA, USA, in 2018. His research interests include wireless power transfer, including coil design and compensation topologies.

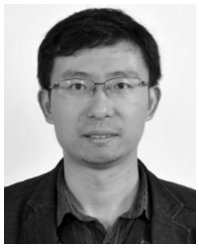

Siqi Li (M'11) received the B.S. and Ph.D. degree in electrical engineering from Tsinghua University, Beijing, China, in 2004 and 2010, respectively.

From 2011 to 2013, he was a Postdoctoral Fellow with the University of Michigan, Dearborn, MI, USA. In 2013, he was with the Faculty of Electric Power Engineering, University of Science and Technology (KUST), Kunming, China, where he is currently an Associate professor with the Department of Electrical Engineering. He is the Director of the Advanced Power Electronics and New Energy Laboratory with the KUST. Since 2018, he has been a Visiting Scholar with the San Diego State University, San Diego, CA, USA. His research interest include battery management system, high performance wired, wireless battery chargers for electric vehicles and solid state transformers.

Chunting Chris Mi (S'00–A'01–M'01–SM'03–F'12) received the B.S.E.E. and M.S.E.E. degrees in electrical engineering from Northwestern Polytechnical University, Xi'an, China, in 1985 and 1988, respectively. He received the Ph.D. degree in electrical engineering from the University of Toronto, Toronto, ON, Canada, in 2001.

He is a Professor and the Chair of Electrical and Computer Engineering and the Director of the Department of Energy-Funded Graduate Automotive Technology Education Center for Electric Drive Transportation, San Diego State University, San Diego, CA, USA. Prior to joining SDSU, from 2001 to 2015, he was with the University of Michigan, Dearborn, MI, USA. His research interests include electric drives, power electronics, electric machines, renewable-energy systems, and electric and hybrid vehicles.